PSFC/JA-08-45

Studies of turbulence and transportation in Alcator C-Mod ohmic plasmas with phase contrast imaging and comparisons with gyrokinetic simulations

L. Lin[1] , M. Porkolab[1] , E.M. Edlund[1], M. Greenwald[1], J.C. Rost[1], N. Tsujii[1], J. Candy[2], R.E.Waltz[2], D. Mikkelsen[3]

June 2009

Plasma Science and Fusion Center
Massachusetts Institute of Technology
Cambridge MA 02139 USA

[1]*M.I.T. Plasma Science and Fusion Center - Cambridge, Massachusetts 02139*

[2]*General Atomics – San Diego, California 92186*

[3]*Princeton Plasma Physics Laboratory – Princeton, NJ 08543*

This work was supported by the U.S. Department of Energy, Grant No. DE-FC02-99ER54512.

Submitted for publication to *Plasma Physics and Controlled Fusion.*

Studies of turbulence and transport in Alcator C-Mod ohmic plasmas with phase contrast imaging and comparisons with gyrokinetic simulations

L Lin, M Porkolab, E M Edlund, J C Rost, M Greenwald, and N Tsujii
Plasma Science and Fusion Center, Massachusetts Institute of Technology, Cambridge, MA 02139, USA

J Candy and R E Waltz
General Atomics, PO Box 85608, San Diego, CA 92186, USA

D R Mikkelsen
Princeton Plasma Physics Laboratory, Princeton, NJ 08543, USA

Abstract

Recent advances in gyrokinetic simulation have allowed for quantitative predictions of core turbulence and associated transport. However, numerical codes must be tested against experimental results in both turbulence and transport. In this paper, we present recent results from ohmic plasmas in the Alcator C-Mod tokamak using phase contrast imaging (PCI) diagnostic, which is capable of measuring density fluctuations with wave-numbers up to 55 cm^{-1}. The experiments were carried out over the range of densities covering the "neo-Alcator" (linear confinement time scaling with density, electron transport dominates) to the "saturated ohmic" regime. We have also simulated these plasmas with the gyrokinetic code GYRO and compared numerical predictions with experimentally measured turbulence through a synthetic PCI diagnostic method. The key role played by the ion temperature gradient (ITG) turbulence has been verified, including measurements of turbulent wave propagation in the ion diamagnetic direction. It is found that the intensity of density fluctuations increase with density, in agreement between simulation and experiments. The absolute fluctuation intensity agrees with simulation within experimental error (+/-60%). In the saturated ohmic regime, the simulated ion and electron thermal diffusivities also agree with experiments after varying the ion temperature gradient within experimental uncertainty. However, in the linear ohmic regime, GYRO does not agree well with experiments, showing significantly larger ion thermal transport and smaller electron thermal transport. Our study shows that although the short wavelength turbulence in the electron temperature gradient (ETG) range is unstable in the linear ohmic regime, the nonlinear simulation with $k_\theta \rho_s$ up to 4 does not raise the electron thermal diffusivity to the experimental level, where k_θ is the poloidal wavenumber and ρ_s is the ion-sound Larmor radius. At the present

time, it is not known if even shorter wavelength turbulence would account for the measured electron transport.

1. Introduction

Early experiments in the Alcator C tokamak observed the "neo-Alcator" scaling of confinement in ohmically heated plasmas, where the energy confinement time (τ_E) is proportional to the line-averaged electron density ($\bar{n}_e$). As the density increases, τ_E saturates and shows a weak dependence on $\bar{n}_e$ [1]. This saturation of confinement was interpreted as evidence of the importance of unstable ion temperature gradient (ITG) turbulence when the ion and electron channels are coupled by collisions at high densities.

Previous studies in the Texas Experimental Tokamak (TEXT) [2] and DIII-D [3] presented experimental evidence for the ITG turbulence in the saturated ohmic regime. Although some nonlinear turbulence calculations were based on the DIII-D conditions, there were no quantitative comparisons of simulated and measured turbulence. In addition, the physics of the neo-Alcator scaling in the linear ohmic regime, where the electron transport dominates, is still not well-understood. A few theoretical transport models based on the finite-β_e universal-mode turbulence [4], the principle of profile consistency [5], or the extreme dissipative trapped electron (DTE) transport scaling [6-8] show a linear relationship between the confinement time and electron density. The theoretical modeling of TEXTOR plasmas suggests the linear ohmic regime is dominated by the dissipative trapped electron mode (TEM), while the saturated ohmic regime is dominated by the ITG mode [9-12]. This interpretation is consistent with the fact that the TEM is stabilized by higher collisionality at a higher density, while the ITG mode is only weakly affected by collisionality. An analogous analysis in ASDEX Upgrade provides results consistent with the above interpretation [13]. Moreover, turbulence measurements in ASDEX Upgrade indicate a transition from TEM to ITG as collisionality increases [14]. However, complete nonlinear gyrokinetic simulations are still necessary for a more quantitative comparison between theory and experiment. As a result, revisiting these ohmic plasmas with experimental turbulence measurements and advanced gyrokinetic simulations is essential in quantitatively understanding electron transport, as well as validating the numerical codes.

In this paper, we report the numerical and experimental studies of turbulence and transport in Alcator C-Mod ohmic plasmas. The phase contrast imaging (PCI) diagnostic [15,16] is used to measure the turbulent density fluctuations. Recent advances in gyrokinetic simulation allow us to quantitatively simulate core turbulence and associated transport [17 - 22]. Moreover, the development of a synthetic PCI diagnostic [23, 24] for GYRO allows for direct and quantitative comparisons between the PCI measurements and numerical predictions. The plasma regimes studied cover both the linear and saturated ohmic regimes, with the goal of resolving a longstanding mystery in transport physics in tokamaks.

This paper is arranged as follows: in Sec. 2, the discharges under study are overviewed; in Sec. 3, the transport analysis with TRANSP are discussed; in Sec. 4, the fluctuation measurements are presented; in Sec. 5, a comparison is given between fluctuation measurements and GYRO predictions; in Sec. 6, a comparison in transport is given between GYRO simulation and TRANSP calculation. Finally, in Sec. 7 the conclusions are presented.

2. Target Plasma Parameters

Our experiments were carried out over a range of densities in the Alcator C-Mod Tokamak [25] covering the "neo-Alcator" (also known as “linear ohmic”) to the "saturated ohmic" regime. As shown in Fig. 1, when the line-averaged electron density ($\bar{n}_e$) is below 0.7×10^{20} m^{-3}, the global confinement time (τ_E) is linearly proportional to the average density, i.e. $\tau_E \propto \bar{n}_e$. After $\bar{n}_e$ increases above 0.8×10^{20} m^{-3}, τ_E saturates and shows a weaker dependence on $\bar{n}_e$. The experiments were conducted with the on-axis toroidal magnetic field (B_ϕ) at 5.2 T and the plasma current (I_p) at 0.8 MA. As examples, the electron density and temperature profiles at $\bar{n}_e = 0.34\times10^{20}$ m^{-3}, $\bar{n}_e = 0.62\times10^{20}$ m^{-3}, and $\bar{n}_e = 0.93\times10^{20}$ m^{-3} are shown in Fig. 2, where the smoothed profiles are obtained by fitting the experimental measurements from the Thomson scattering (n_e, T_e) and electron cyclotron emission (T_e) diagnostics [26]. It is seen that the experimental uncertainty of the electron density and temperature measurements is typically ~15%. To further reduce the statistical uncertainty in the data analysis and processing, large data sets are used from steady discharges. All the data, including the plasma equilibrium and fluctuation measurements used in the paper, are averaged over the steady phase (~0.4 sec) of the discharge. These averaged profiles, as shown in Fig. 3, are used in the following transport analyses and gyrokinetic simulations.

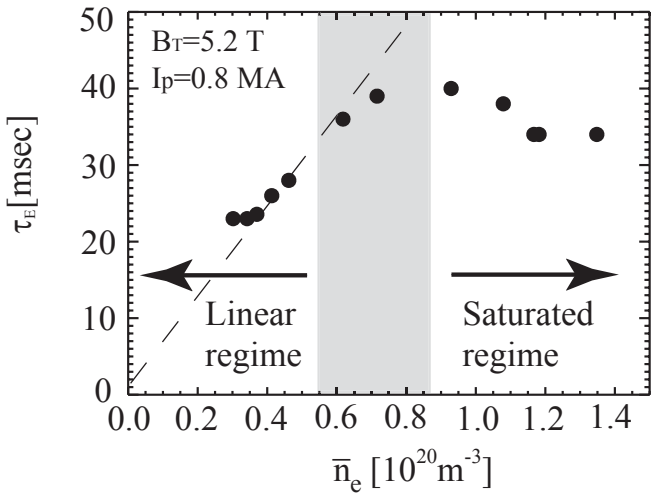

Figure 1. Energy confinement time τ_E versus line-averaged density $\bar{n}_e$. The shaded region represents the transition between the linear ohmic and saturated ohmic regime.

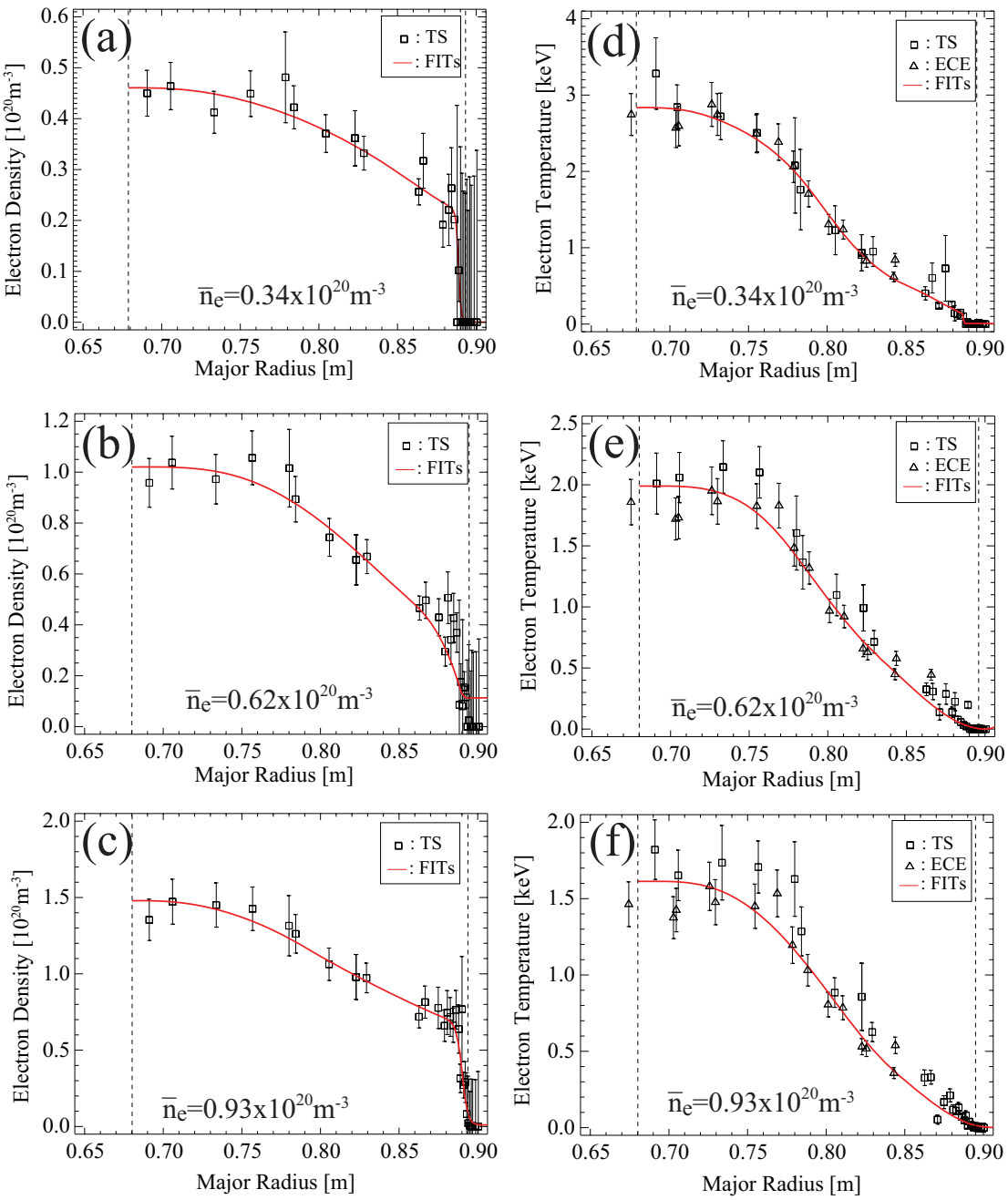

Figure 2. Electron density and temperature profiles at $\bar{n}_e = 0.34\times10^{20}$ m^{-3}, $\bar{n}_e = 0.62\times10^{20}$ m^{-3} and $\bar{n}_e = 0.93\times10^{20}$ m^{-3}. (a)-(c) are electron density profiles and (d)-(f) are electron temperature profiles, where the electron density profiles are measured by the Thompson (TS) diagnostic and the electron temperature profiles are measured by the TS and electron cyclotron emission (ECE) diagnostics. The solid curve is a fit to the experimental measurements using FiTs. Two vertical dashed lines on each plot correspond to the magnetic axis and the last closed flux surface (LCFS), respectively.

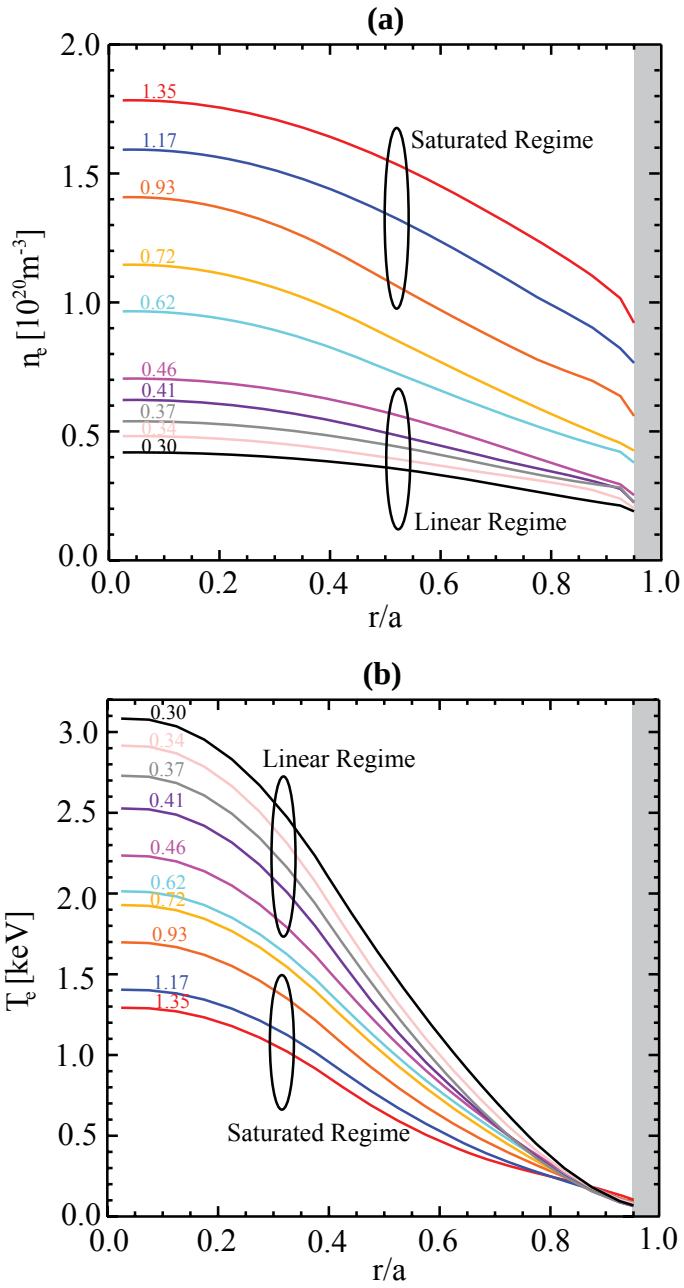

Figure 3. Electron density (a) and temperature (b) profiles at different densities, where the line-averaged density $\bar{n}_e$ of each profile is labeled.

3. Transport Analysis with TRANSP

In our studies, the thermal transport characteristics are determined with the TRANSP [27] code, which calculates the local thermal diffusivities from the energy balance equations. TRANSP is also used to determine these unmeasured plasma parameters, such as ion temperature profiles, which are necessary in the gyrokinetic simulation. In Alcator C-Mod, the high resolution X-ray spectrometer (Hirex) [28] was used to measure ion temperature profiles but these measurements were not always available. Thus, the ion temperature profiles used here are calculated from the neutron measurement. TRANSP uses experimental electron density and temperature profiles and a multiplier on the electron diffusivity χ_e to obtain an ion temperature profile consistent with the neutron measurement [29]. This modeling is based on two assumptions: first, the ion temperature profile is Gaussian with a width similar to that of the electron temperature profile; second, the ion density is calculated from the electron density using a flat Z_{eff} profile. In the TRANSP analysis presented in this paper, the input Z_{eff} is calculated from the neoclassical resistivity [30]. To estimate the uncertainty of the modeled ion temperature T_i and its gradient ∇T_i, the calculated Z_{eff} and measured neutron rate is varied by ±15%. The resulting changes of the modeled T_i and ∇T_i are as much as 10% and 30%, respectively. The resulting change on the dimensionless parameter $a/L_{Ti} = -(a/T_i)(dT_i/dr)$ is as much as 30%.

Approaching the center of the plasma column, the heat flux Q goes to zero, which implies that the temperature gradient goes to zero, i.e. $\nabla T \to 0$. Consequently, it is difficult to compute the thermal diffusivity (χ), since $\chi \propto Q/\nabla T$. Near the plasma edge, the errors in the electron density and temperature profiles are especially large. Therefore, the focus of the TRANSP analysis is the plasma core, which is taken to be in the range of $r/a \in [0.2, 0.8]$ in this paper. The thermal diffusivities from the TRANSP analysis at low ($\bar{n}_e = 0.34\times10^{20}$ m^{-3}), medium ($\bar{n}_e = 0.62\times10^{20}$ m^{-3}), and high ($\bar{n}_e = 0.93\times10^{20}$ m^{-3}) density plasmas are shown in Fig. 4, where the lowest density plasma corresponds to the linear ohmic regime where τ_E is linearly proportional to $\bar{n}_e$. The highest density plasma corresponds to the saturated ohmic regime where τ_E is saturated. The medium density plasma represents the transition from the linear to saturated

ohmic regime. As the density increases, the electron thermal diffusivity χ_e decreases, but the ion thermal diffusivity χ_i increases slowly; the effective thermal diffusivity

$$\chi_{eff} \equiv \frac{n_e \chi_e \nabla T_e + n_i \chi_i \nabla T_i}{n_e \nabla T_e + n_i \nabla T_i}$$

also decreases. We also note that χ_i is much lower than χ_e in the linear ohmic regime and becomes comparable to χ_e in the saturated ohmic regime. This indicates that the electron and ion transport channels are decoupled at the low density and the ohmic power is lost mainly through the electron channel.

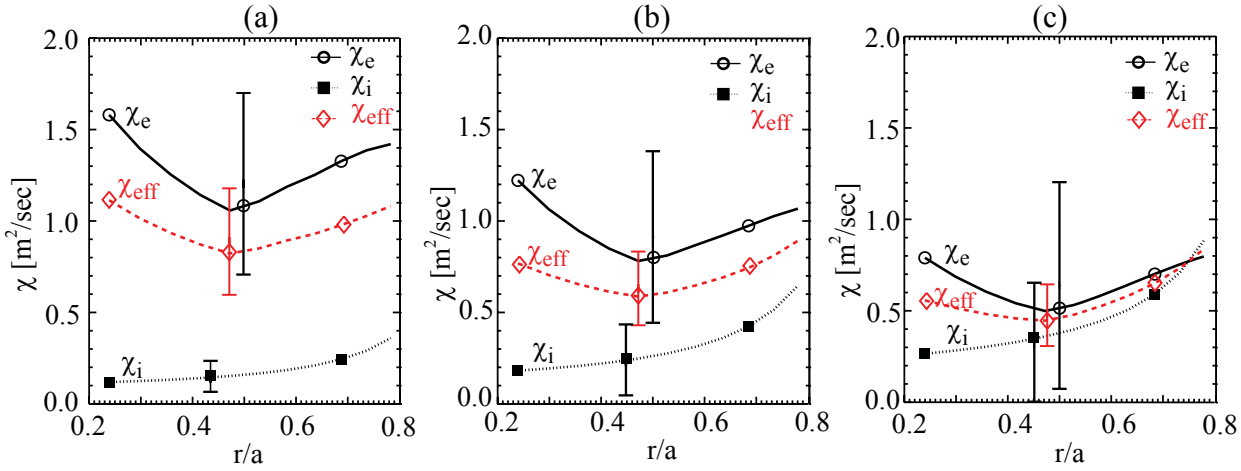

Figure 4. TRANSP calculated thermal diffusivities for ohmic plasmas at the line-averaged density of (a) $\bar{n}_e = 0.34\times10^{20}$ m^{-3}, (b) $\bar{n}_e = 0.62\times10^{20}$ m^{-3} and (c) $\bar{n}_e = 0.93\times10^{20}$ m^{-3}.

4. Fluctuation Measurements

To study the change in turbulent transport as the density varies in ohmic plasmas, it is of great importance to measure the change in turbulent fluctuations. In Alcator C-Mod, the phase contrast imaging (PCI) diagnostic has been used to monitor these fluctuations. The PCI diagnostic measures the line-integrated density fluctuations along the 32 vertical chords of the CO_2 laser beam as shown in Fig. 5. The signals are detected by 32 photoconductive HgCdTe linear detectors. A more detailed discussion of the PCI diagnostic can be found in Refs. [15, 16,31,32]. The signal of each chord takes the form of $s_j = \int \tilde{n}(R_j, z)dz$, where $\tilde{n}$ is the electron density fluctuation, z is the vertical coordinate, R_j is the major radius coordinate of each vertical chord, and j is the channel number. Through the Fourier decomposition, both the frequency and wavenumber of the measured fluctuations can be extracted. In general, the Alcator C-Mod PCI system is capable of measuring turbulent density fluctuations in the wavenumber range of 0.5-55 cm^{-1} and in the frequency range of 2 kHz to 5 MHz. An absolute calibration has been obtained by using the PCI system to measure the density perturbations induced by calibrated sound waves [33].

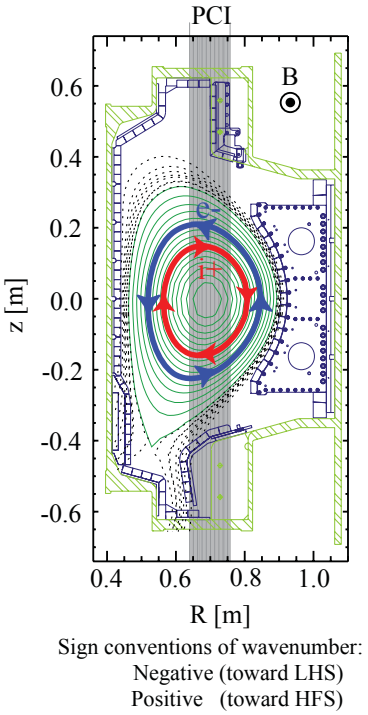

Figure 5. Laser beam path in the Alcator C-Mod PCI system. The sign convention of wavenumber in this paper is also indicated at the bottom, where the positive (negative) wavenumber corresponds to the mode propagating toward high (low) field side.

The frequency spectra of a single chord PCI measurement are shown in Fig. 6, where the density fluctuation intensity decays as the frequency increases. A linear fit $\log P_f = -A_f \log f + B_f$ is used to estimate the decay rate, where P_f is the fluctuation intensity of the frequency spectra. The decay rate in the lower frequency range of 20-80 kHz, where $A_f \approx 1.5 \pm 0.3$, is smaller than that in the higher frequency range of 100-250 kHz, where $A_f \approx 4.2 \pm 0.7$, depending on densities. We also note a knee exists in the frequency spectrum when the density is above $0.7 \times 10^{20}\,\mathrm{m}^{-3}$. As the density decreases, the location of this knee in frequency tends to move toward higher frequency. However, the knee feature becomes less pronounced when the density is below $0.7 \times 10^{20}\,\mathrm{m}^{-3}$. Currently, the cause and influence of this feature is not well understood.

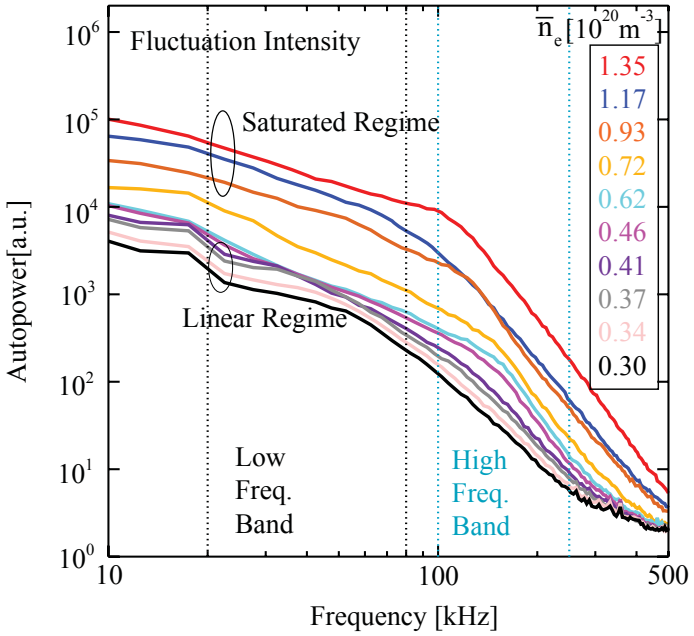

Figure 6. Frequency spectra of a PCI core channel (14) at different densities. The spectra are averaged over 400 ms and shown with a 5 kHz frequency resolution.

As shown in Fig. 5, although the turbulent wave propagates only in one direction (electron or ion diamagnetic direction), it intersects with the PCI laser beam twice (once at the top and once at the bottom) and is measured as two oppositely propagating waves on the PCI wavenumber spectra. Since the conventional PCI configuration measures the line-integrated density fluctuations evenly along the vertical chord, it cannot differentiate contributions from the top or

bottom. Consequently, the conventional PCI configuration cannot resolve the direction of propagation of the measured turbulence. Recent upgrades have enabled the Alcator C-Mod PCI system to partially localize the longer wavelength turbulence in the ion temperature gradient (ITG) and trapped electron mode (TEM) regimes. This localizing technique relies on a masked phase plate, which introduces a weight function $w(z)$ to the PCI signal in the line integration, i.e., $\int w(z)\tilde{n}(R_j, z)dz$. As a result, the localizing PCI can differentiate contributions from the top or bottom by setting $w_{z>0} > w_{z<0}$ (preferentially top view) or $w_{z>0} < w_{z<0}$ (preferentially bottom view), thereby resolving the direction of propagation. [16] In the studies presented in this paper, the PCI system is set to view the bottom column plasma preferentially, i.e. $w_{z<0} > w_{z>0}$. According to the sign convention of wavenumbers shown in Fig. 5, the positive wavenumber corresponds to the turbulent waves propagating in the ion diamagnetic direction, while the negative wavenumber corresponds to those propagating in the electron diamagnetic direction in the laboratory frame. Figure 7 shows the frequency/wavenumber of the PCI measurement at $\bar{n}_e = 0.93\times10^{20}$ m^{-3} in the saturated ohmic regime. The measurement shows that the fluctuations in the higher frequency range of 80-250 kHz propagate in the ion diamagnetic direction in the laboratory frame, where the experimentally measured frequency (f_{lab}) equals to the mode frequency (f_{mode}) plus the Doppler shift due to E×B drift velocity (f_{ExB}), i.e. $f_{lab} = f_{\text{mode}} + f_{\text{E×B}}$. Although the radial electric field is not well measured for the considered plasmas, the available measurements indicate that the background Doppler rotation is not enough to reverse the mode propagating direction of the turbulence with the wavenumbers in the ITG and TEM regime. Therefore, this measurement also shows that the fluctuations in the higher frequency range of 80-250 kHz propagate in the ion diamagnetic direction in the plasma frame.

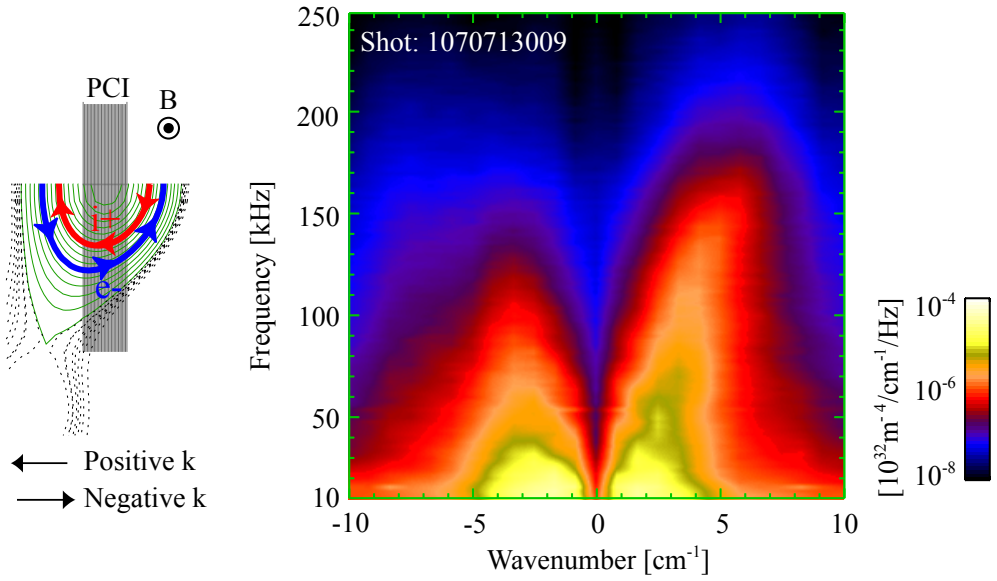

Figure 7. Frequency/wavenumber spectra of the PCI measurement at $\bar{n}_e = 0.93\times10^{20}$ m^{-3} in the saturated ohmic regime. The PCI diagnostic is set to preferentially view the bottom plasma.

It is very tempting to seek correlation between the overall fluctuation intensities measured by PCI and the global confinement time. The PCI measurements can be normalized to the line-integrated density for an estimated fluctuation level. The results are shown in Fig. 8. Here the normalized density fluctuation is shown in arbitrary units, since we only focus on its variation as the density changes. Currently, the experimental error of the PCI measurements mainly comes from the uncertainty of calibration, which provides a conversion factor to express fluctuation intensity ($\left|\int \tilde{n}_e dl\right|^2$) in the scale of m^{-4}. When the measurements are expressed in the real scale, the uncertainty is +/-60%. However, when the comparison is performed in arbitrary units between measurements with the same diagnostic performance, the uncertainty is typically below 10%. As shown in Fig. 8(a), in the linear ohmic regime $\bar{n}_e \lesssim 0.7\times10^{20}$ m^{-3}, the relative density fluctuation intensity in the frequency range of 20-80 kHz decreases as density increases; this shows some correlation with the confinement time scaling where $\tau_E \propto \bar{n}_e$. However, there is no significant difference for relative density fluctuation in the electron and ion diamagnetic direction in the laboratory frame. This suggests the PCI measurement below 80 kHz might be localized at the plasma edge, where the turbulence propagating in the ion and electron diamagnetic directions may be comparable. An alternative explanation is that low frequency modes coming from the plasma core and the edge are mixed together in a way we cannot

separate them. The masked PCI has resolved that fluctuations above 80 kHz are dominated by the mode propagating in the ion diamagnetic direction in both the linear and saturated ohmic regimes, as shown in Fig. 8(b). This dominance becomes more apparent in the saturated ohmic regime as density increases, which indicates that ITG becomes more significant as density increases where electrons and ions are more coupled.

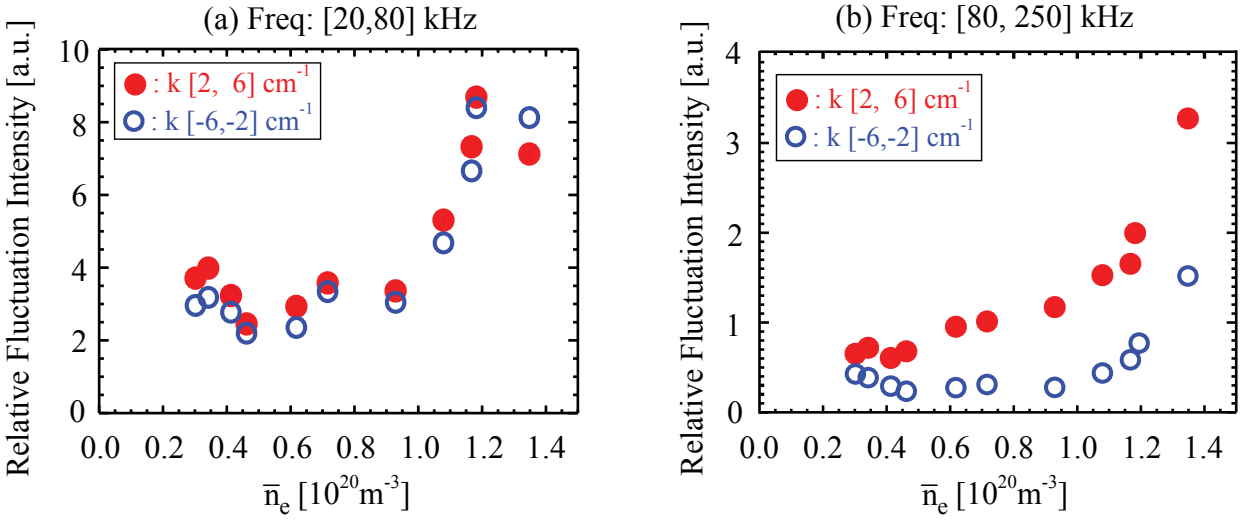

Figure 8. Relative density fluctuation intensity level vs. the line-averaged density (red dot: integrated over the wavenumber range of [2, 6] cm^{-1}, corresponding to the mode propagating in the ion diamagnetic direction for the preferentially bottom view configuration of PCI; blue open circle: integrated over the wavenumber range [-6, -2] cm^{-1} corresponding to the mode propagating in the electron diamagnetic direction for the preferentially bottom view configuration of PCI) (a) integrated over the frequency range of 20-80 kHz; (b) integrated over the frequency range of 80-250 kHz

We also want to point out that the above comparison between the estimated density fluctuation level and confinement time as the density varies is limited for two reasons. First, PCI measures line-integrated electron density fluctuations (including both plasma core and edge) and phase cancellation might be important in the line-integration of density fluctuations, which makes it difficult to directly relate the PCI measurement to the local transport. Second, since turbulence-driven transport also depends on other unknown plasma parameters and their correlations (such as potential and temperature fluctuations), large density fluctuations do not always correspond to large thermal transport. To provide better understanding of experimental measurements, we have

also simulated turbulence with the GYRO code [17, 18], which quantitatively relates the fluctuation spectra to transport.

5 Turbulence Studies with GYRO

To further explore the nature of turbulence and the drive mechanism of thermal transport, we have used GYRO to simulate turbulence and transport. GYRO is a physically comprehensive global code which solves the nonlinear 5-D gyrokinetic-Maxwell equations for both ions and electrons in a local (flux-tube) or 'global' radial domain [17, 18]. The input file is prepared from the output of TRANSP [27] using the data translator (trgk) developed at PPPL. The electrostatic approximation is assumed for all the simulations presented in this paper, since we verified that the contributions from electromagnetic fluctuations are negligible in our simulation of the low-β ($\beta \lesssim 0.1\%$) C-Mod plasmas.

It is apparent that the unprocessed simulated density fluctuations cannot be directly compared with the PCI measurements, since PCI measures the line-integrated density fluctuations which is heavily influenced by the phase cancellations and the variation of plasma profiles along the integrating line. This makes the synthetic PCI crucial when comparing simulations with experimental measurements[23]. The synthetic PCI post-analyzes the output of the global GYRO simulations and emulates the PCI measurements by line-integrating the electron density fluctuation along the PCI beam path, where the system response is also included. After obtaining a synthetic PCI signal, the same analysis package as the experimental data is used for spectral analysis.

All simulations are performed with the real mass ratio ($m_i / m_e \approx 3600$) and kinetic electrons. Unless otherwise specified, the nonlinear global GYRO simulations in this paper cover the plasma domain of $0.4 \lesssim r/a \lesssim 0.8$ and include 16 modes evenly spaced between $0.0 \lesssim k_\theta \rho_s \lesssim 1.0$ at the center of the simulated domain, where k_θ is the wavenumber in the poloidal direction, $\rho_s = c_s / \Omega_i$ is the ion-sound Larmor radius, $c_s = (T_e / m_i)^{1/2}$ is the ion sound speed, $\Omega_i = eB_\phi / (m_i c)$ is the ion cyclotron frequency, and m_i is the ion mass. Figure 9 shows the synthetic PCI spectra from the GYRO simulation of the plasma at $\overline{n}_e = 0.93 \times 10^{20}$ m^{-3} in the

saturated ohmic regime. As shown in Fig. 9(a) where the Doppler shift corresponding to the average poloidal flow is not accounted for, the fluctuation with the positive wavenumber dominates, consistent with the ITG turbulence. Here, an average poloidal flow $v_{ExB} = 2$ km/sec is chosen to match the phase velocity of the broadband turbulence above 80 kHz in the PCI measurements. This value corresponds to $E_r \simeq 10$ kV/m , which gives a typical Doppler shifted frequency of ~ 64 kHz for $k_\theta \sim 2$ cm^{-1}. With the assumed Doppler shift the synthetic spectra, as shown in Fig. 9(b), are similar to the experimental measurements (see Fig. 7).

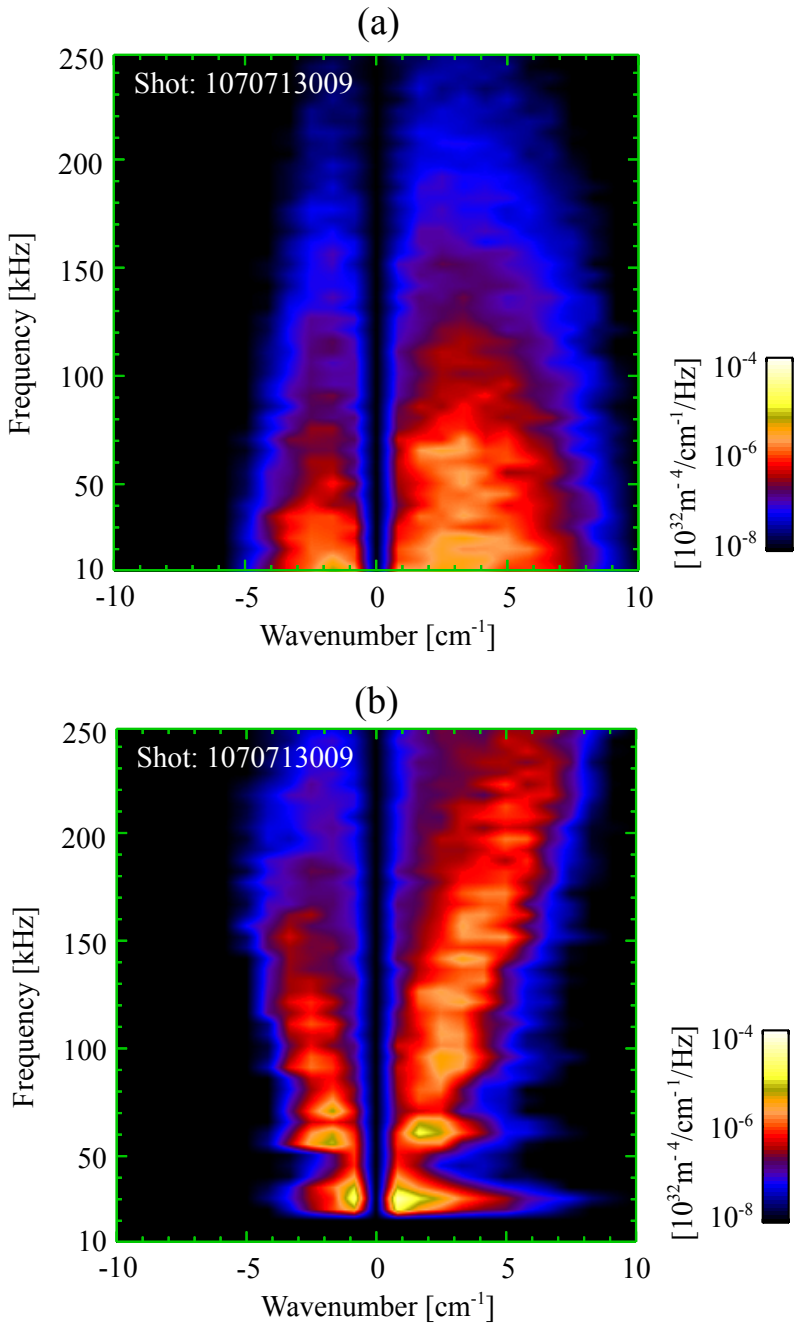

Figure 9. Synthetic PCI spectra at $\bar{n}_e = 0.93\times10^{20}$ m^{-3} : (a) no Doppler shift; (b) adding $v_{E\times B} = 2$ km/sec for Doppler shift.

It is useful to integrate the frequency/wavenumber spectra (as shown in Fig. 9b) over a frequency range for a quantitative comparison between experiments and simulations. The integrating frequency range is chosen to be 80-250 kHz, where the PCI measurement is dominated by the core turbulence (see Sec. 4). As shown in Fig. 10, the wavenumber spectrum of density

fluctuations in the 80-250 kHz range quantitatively agrees with GYRO simulation in the core ($0.4 \lesssim r/a \lesssim 0.8$). The convergence studies with different mode grid number N_n and toroidal mode separation Δn are shown in Fig. 10(a): (1) $N_n = 16$, $\Delta n = 10$; (2) $N_n = 10$, $\Delta n = 12$; (3) $N_n = 20$, $\Delta n = 10$. These simulations agree with experimental measurements within the experimental uncertainty (+/-60%). The simulations with different ion temperature profiles at $\bar{n}_e = 0.93\times10^{20}$ m^{-3} are shown in Fig. 10(b). Three ion temperature profiles are used: (1) Modeled T_i with TRANSP to match the neutron measurement; (2) $T_i = 0.8\times T_e$; (3) $T_i = T_e$. The simulated wavenumber spectra with different ion temperature profiles all agree with each other, as well as experimental measurements.

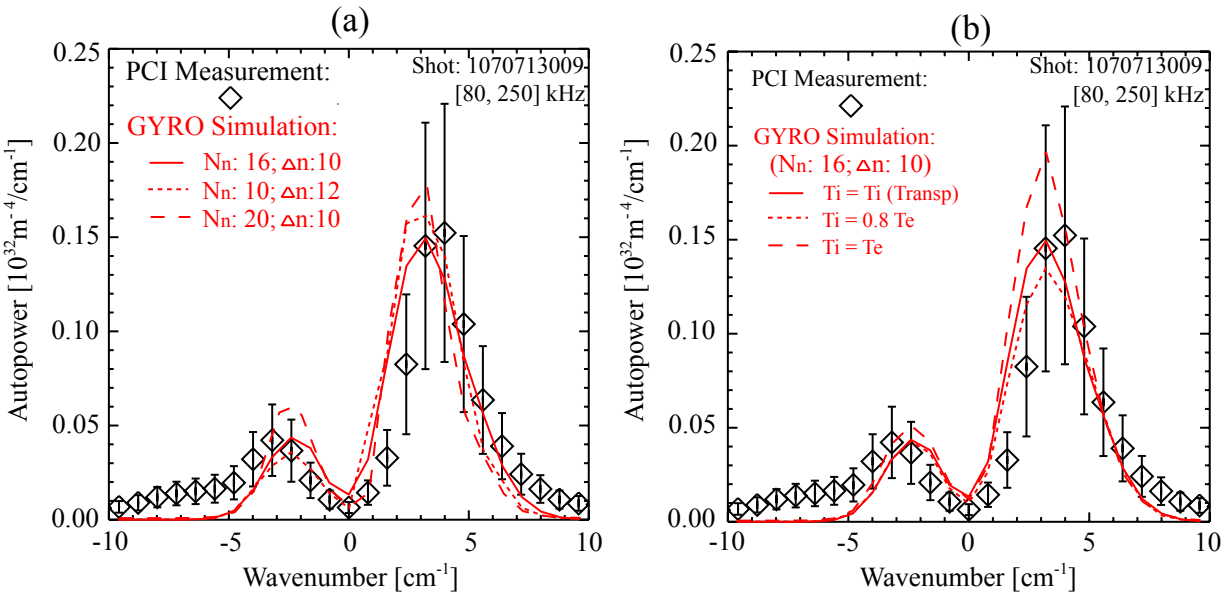

Figure 10. (a) Comparison of PCI measurements with GYRO simulations with different set of toroidal mode numbers at $\bar{n}_e = 0.93\times10^{20}$ m^{-3}. (b) Comparison of PCI measurements with GYRO simulations with different ion temperature profiles at $\bar{n}_e = 0.93\times10^{20}$ m^{-3}:.

The measured turbulence in the 50-80 kHz range propagates in the ion diamagnetic direction (see Fig. 7). After including the contribution of turbulence in the 50-80 kHz range, the simulated wavenumber spectra in the core ($0.4 < r/a < 0.8$; Fig. 9b) still agrees with the measured spectra within the experimental uncertainties (+/-60%) although the agreement is not as good as in Fig. 10. However, the PCI is a line-integrated density fluctuation diagnostic, where both core and

edge turbulence contributes to the measured spectra. The induced ExB Doppler shift is relatively smaller since the turbulence in the 50-80 kHz range has lower wavenumbers than those above 80 kHz (see Fig. 7); thus, the core turbulence below 80 kHz is still mixed together with the edge turbulence.

Simulations of ohmic plasmas at other densities and similar analysis have been carried out. At lower densities, similar spectral shapes were obtained but with progressively lower intensities. A summary of the results as a function of density is shown in Fig. 11. It is seen that the integrated density fluctuation intensities in the frequency range of 80-250 kHz are quantitatively consistent with a series of GYRO global simulations.

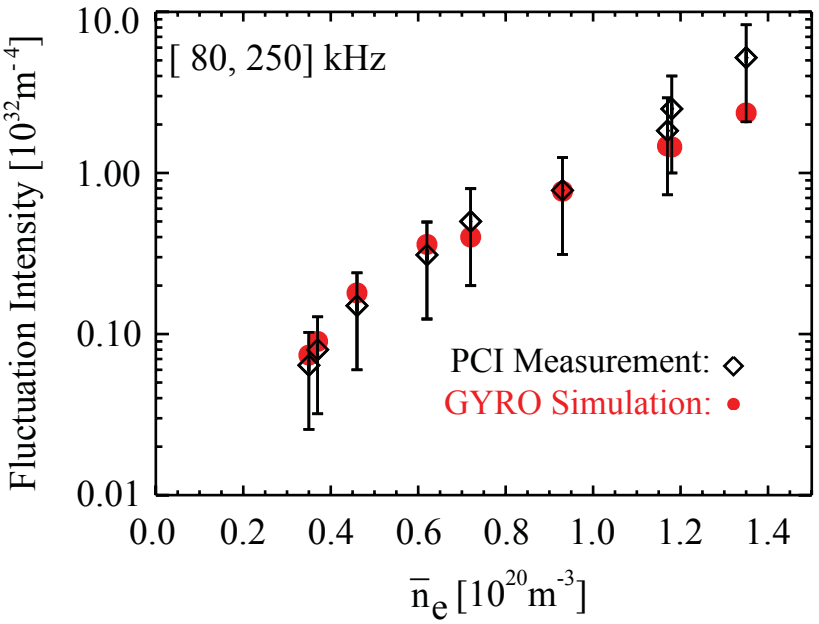

Figure 11. Comparison of the simulated fluctuation intensity ($\left|\int \tilde{n}_e dl\right|^2$) in the frequency range of 80-250 kHz with experimental measurements at various densities, where the fluctuation intensity is shown in the scale of 10^{32}m^{-4}.

For the line-integrated fluctuation measurements, the background density is characterized by a profile instead of a constant. Thus, it is difficult to relate the PCI measurements to the local relative fluctuation intensity. However, it is still tempting to deduce the density fluctuation level ($\tilde{n}_e / n_e$) from the fluctuation intensity ($\left|\int \tilde{n}_e dl\right|^2$) as shown in Fig. 11 through $\tilde{n}_e / n \sim \left|\int \tilde{n}_e dl\right| / (\bar{n}_e L)$. Considering a reasonable integration length of $L \sim 5$ cm, we find that $\tilde{n}_e / n \sim 0.2\%$ (see Fig. 11). However, the deduced $\tilde{n}_e / n_e$ through the above approaches does not provide the right local value of $\tilde{n}_e / n_e$ or contain meaningful physics. The reasons are twofold. First, the PCI diagnostic measures the line-integrated density fluctuation. The phase cancellation during the line-integration will cause $|\int \tilde{n}_e dl| < \int |\tilde{n}_e| dl|$. Thus, the actual value of $\tilde{n}_e / n_e$ is likely to be much larger than the estimated one. Second, the integrating frequency band in Fig. 11 is selected to be 80-250 kHz, where the measured fluctuations are dominated by the core-localized turbulence. A proper calculation of $\tilde{n}_e / n_e$ should include the contribution of the fluctuations below 80 kHz. However, the measured fluctuations below 80 kHz are mixed together with the edge-localized turbulence and therefore the core contribution cannot be properly distinguished. However, we can state from the GYRO simulations that locally, $\tilde{n}_e / n_e \sim 1-3\%$ depending on densities in the range of Fig. 11.

6. Simulated Transport with GYRO

GYRO also simulates the thermal transport due to the turbulent fluctuations. It is well known that $a/L_{Ti} = -(a/T_i)(dT_i/dr)$ is a crucial parameter in transport analysis (see e.g. [18, 34, 35]). To quantitatively investigate the impact of a/L_{Ti} on thermal transport, we have carried out extensive sensitivity studies at the higher density ($\overline{n}_e = 0.93\times10^{20}$ m^{-3}), the medium density ($\overline{n}_e = 0.62\times10^{20}$ m^{-3}) and the lower density ($\overline{n}_e = 0.34\times10^{20}$ m^{-3}). The most relevant nominal input parameters at the center of the global simulations are summarized in Table 1. For each density, the key parameter $a/L_{Ti} = -(a/T_i)(dT_i/dr)$ is reduced by a factor of $\varepsilon = 0.1$, 0.2, and 0.3. The nonlinear global GYRO electrostatic simulations include 16 modes evenly spaced between $0.0 \lesssim k_\theta \rho_s \lesssim 1.0$ at the center of the simulation domain and cover the plasma of $0.4 \lesssim r/a \lesssim 0.8$ with the real mass ratio ($m_i/m_e \approx 3600$) and kinetic electrons. In addition, we have also estimated the uncertainties of the experimental thermal diffusivities by scaling the electron temperature and ion temperature profiles by ±15% ($T_i \to 0.85T_i$, $T_e \to 0.85T_e$; $T_i \to 0.85T_i$, $T_e \to 1.15T_e$; $T_i \to 1.15T_i$, $T_e \to 0.85T_e$; $T_i \to 1.15T_i$, $T_e \to 1.15T_e$) and feeding the scaled profiles into the TRANSP. The variations of the calculated diffusivities are used to estimate the experimental uncertainties. The comparison between the experimental χ_{eff} and simulated χ_{eff} with GYRO averaged over $r/a \in [0.4, 0.8]$ is shown in Fig. 12. The simulated χ_{eff} agrees with the experimental measurements after a ~20% reduction of a/L_{Ti}, where the simulated fluctuation intensities still agree with experiments within the experimental uncertainty (+/-60%).

Table 1. The input parameters at the center ($r/a = 0.63$) of the global simulations.

$\bar{n}_e$ [10^{20} m^{-3}]	0.34	0.62	0.93
Aspect Ratio R/a	3.115097	3.118168	3.128948
Elongation κ	1.221334	1.233673	1.203849
$s_\kappa = (r/\kappa)\partial\kappa/\partial r$	0.164005	0.172129	0.097774
Triangularity δ	0.085349	0.091244	0.061823
$s_\delta = r\partial\delta/\partial r$	0.182362	0.194366	0.109060
Safety factor q	1.410419	1.494749	1.152875
$\hat{s} = (r/q)\partial q/\partial r$	1.625332	1.585791	1.097617
$\nu_{ei}/(c_s/a)$	0.050849	0.161528	0.194468
a/L_{T_i}	3.612313	3.617833	2.370893
a/L_{T_e}	3.451792	3.139384	2.559236
a/L_{n_i}	0.850856	1.171108	0.904540
a/L_{n_e}	0.850856	1.171108	0.904540
T_i/T_e	0.385030	0.595595	0.727208

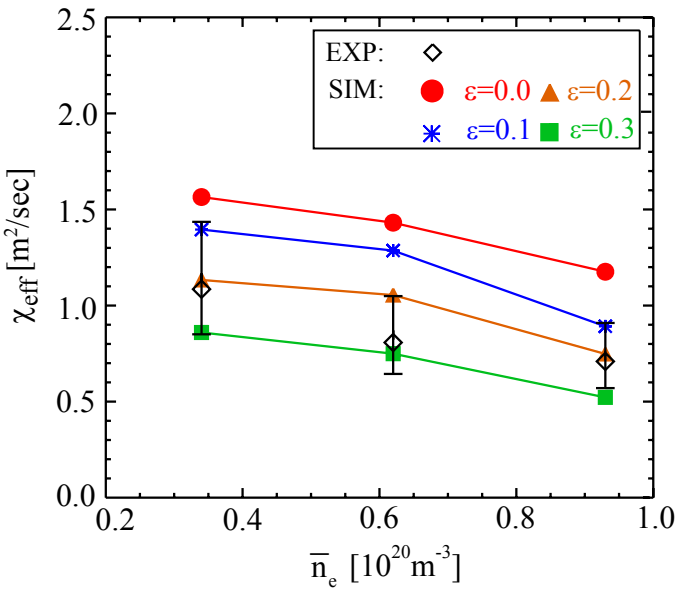

Figure 12. Comparison between the simulated and experimental effective thermal diffusivities (χ_{eff}), where ε is the reduction factor of $a/L_{Ti} = -(a/T_i)(dT_i/dr)$ in simulations.

At the lowest density, TRANSP shows that experimental χ_e is well above χ_i; hence, we can analyze χ_e and χ_i separately instead of χ_{eff}. The comparisons between the simulated and experimental χ_e and χ_i are shown in Fig. 13. At the highest density ($\bar{n}_e = 0.93\times10^{20}$ m^{-3}) in the saturated ohmic regime, both simulated χ_e and χ_i agree with experimental measurements after reducing a/L_{Ti} by 20%. However, at the lower density $\bar{n}_e = 0.62\times10^{20}$ m^{-3} and $\bar{n}_e = 0.34\times10^{20}$ m^{-3} in the linear ohmic regime, the simulated χ_e and χ_i do not agree with experimental measurements.

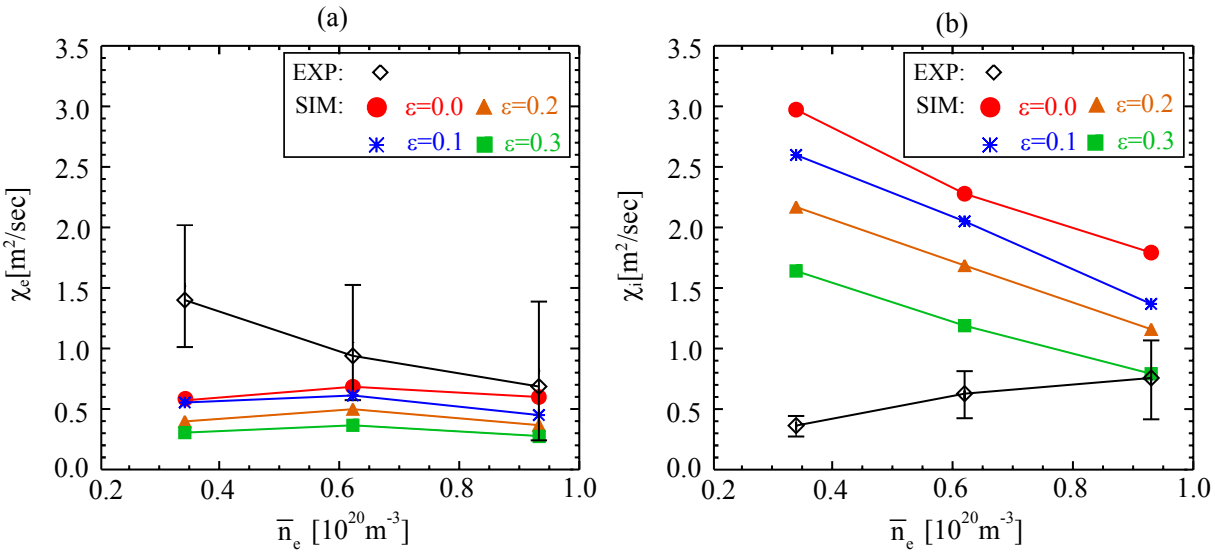

Figure 13. Comparison between the simulated and experimental thermal diffusivities: (a) electron thermal diffusivity χ_e; (b) ion thermal diffusivity χ_i, where ε is the reduction factor of a/L_{Ti} in simulations and $\chi_{e,i}$ is averaged over the domain of $r/a \in [0.4, 0.8]$.

The simulated ion thermal diffusivity can be reduced to the experimental level by further reducing a/L_{Ti} and/or adding E×B shear [36], but by doing so we find that the simulated electron thermal diffusivity is further reduced below the experimental level.

It is well known that the steep density gradient can further destabilize the TEM turbulence. Thus, we have also numerically studied the impact of varying the density gradient, at the lowest density plasma $\bar{n}_e = 0.34\times10^{20}$ m^{-3}. The nonlinear global GYRO simulations include 16 modes evenly spaced between $0.0 \lesssim k_\theta \rho_s \lesssim 1.0$ and cover the plasma domain of $0.4 \lesssim r/a \lesssim 0.8$ with the real mass ratio ($m_i/m_e \approx 3600$) and kinetic electrons. The value of the dimensionless parameter $a/L_{ne} = -(a/n_e)(dn_e/dr)$ at $r/a = 0.63$ is used to quantify the variation of the density gradient. The value of $a/L_{ni} = -(a/n_i)(dn_i/dr)$ is varied together with a/L_{ne}, i.e. $a/L_{ni} = a/L_{ne}$. To also study the impact of the temperature gradient as the density gradient varies, two extra simulations in addition to the base case are performed for each a/L_{n_e}, where a/L_{T_i} is reduced by a factor of 0.2 and 0.4. The comparison between the experimental $\chi_{e,i}$ and simulated $\chi_{e,i}$ with

GYRO averaged over $r/a \in [0.4, 0.8]$ is shown in Fig. 14. It is found that the density gradient variation has a weak impact on turbulent transport. The simulated electron thermal diffusivity χ_e can only be raised to the experimental level after increasing a/L_{n_e} by at least a factor of 2 where the TEM turbulence becomes significant. The simulated ion transport χ_i always remains above the experimental level. The impact of the variation of the ion temperature gradient a/L_{T_i} on the turbulent transport becomes weaker when the TEM turbulence gets stronger. Since an increase of a/L_{n_e} by a factor of 2 is beyond the experimental uncertainty, significant thermal transport contribution from the TEM turbulence is not likely for the measured temperature and density profiles.

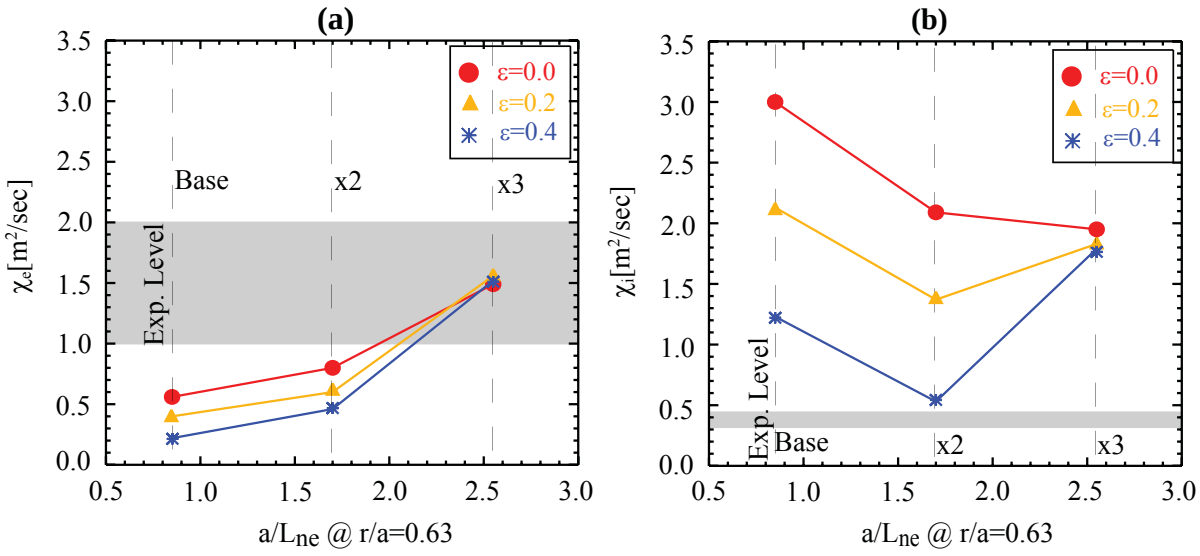

Figure 14. Impact of varying a correction factor applied to the measured density gradient on the simulated thermal diffusivities at $\bar{n}_e = 0.34\times10^{20}$ m^{-3}: (a) electron; (b) ion, where ε is the reduction factor of a/L_{Ti} used in the simulations. Both χ_e and χ_i are averaged over the domain of $r/a \in [0.4, 0.8]$. The shaded regime corresponds to the experimental level of χ_e and χ_i, respectively.

The collisions also play an important role in TEM, since the pitch angle scattering can scatter the trapped particles into the passing domain and vice versa. To explore the impact of the

collisionality, we have a series of linear stability runs in the plane of a/L_{Ti} - $\nu_{ei}/(c_s/a)$, where ν_{ei} is the electron-ion collisional frequency and c_s is the ion sound speed. The other input parameters are taken from $r/a=0.63$ at the lowest density plasma with $\bar{n}_e = 0.34\times10^{20}$ m^{-3} as in Table 1. These linear runs cover $0.0 \le a/L_{Ti} \le 4.0$ and $0.0 \le \nu_{ei}/(c_s/a) \le 0.1$. Because linear GYRO uses an initial value approach, it is restricted to only resolve the fastest growing (or least damped) eigenmode. The results are shown in Fig. 15. As shown in Fig. 15(a), for the experimental collisionality ($\nu_{ei}/(c_s/a) \sim 0.05$), TEM becomes the most unstable mode when $a/L_{Ti} \le 1.8$, which corresponds to a 50% reduction of the experimental base case. As shown in Fig. 15(b), the collisionality shows a strong stabilization of the TEMs but only a weak impact on the ITG modes. For the experimental collisionality ($\nu_{ei}/(c_s/a) \sim 0.05$), the growth rate ($\sim 320\times10^3$ sec^{-1}) of the ITG mode at $a/L_{Ti} \sim 3.6$ is larger than the growth rate of the TEMs $\sim 200\times10^3$ sec^{-1} at $a/L_{Ti} \sim 0$. Thus, the thermal transport from the TEMs is expected to be less significant than the ITG modes. For illustrative purposes, a nonlinear flux-tube simulation has been performed at $a/L_{Ti} \sim 0.72$ (well below the experimental value) and $\nu_{ei}/(c_s/a) \sim 0.05$ where the TEM is the most unstable mode. The flux-tube simulation includes 20 modes up to $k_\theta \rho_s = 2.0$ with the real mass ratio ($m_i/m_e \approx 3600$) and kinetic electrons. The simulated electron thermal diffusivity χ_e is 0.08 m^2/sec, which is significantly below the experimental level of 1.5 ± 0.5 m^2/sec.

To quantitatively study the impact of collisionality on the simulated thermal transport, we have performed nonlinear local simulations with different ν_{ei} input. Three cases are considered: $\nu_{ei}/(c_s/a) = 0.01$, $\nu_{ei}/(c_s/a) = 0.05$, and $\nu_{ei}/(c_s/a) = 0.10$, where $\nu_{ei}/(c_s/a) = 0.05$ corresponds to the experimental measurements at $r/a = 0.63$. The other input parameters are taken from $r/a = 0.63$ at the lowest density plasma with $\bar{n}_e = 0.34\times10^{20}$ m^{-3} as in Table 1. The local simulation includes 20 modes up to $k_\theta \rho_s = 2.0$ with the real mass ratio ($m_i/m_e \approx 3600$) and kinetic electrons. The results of the nonlinearly simulated thermal diffusivities at various ν_{ei} are summarized in Table 2, where both χ_e and χ_i increase as ν_{ei} decreases. The simulated

electron thermal diffusivity χ_e remains below the experimental level of 1.5 ± 0.5 m^2/sec as ν_{ei} varies, while the simulated ion thermal diffusivity χ_i remains well above the experimental level of 0.4 ± 0.1 m^2/sec.

Table 2: Simulated χ_e and χ_i at various ν_{ei}, where $\nu_{ei}/(c_s/a) = 0.05$ corresponds to the calculated ν_{ei} based on the experimental measurements. The other plasma parameters are taken from $r/a = 0.63$ at the lowest density plasma with $\bar{n}_e = 0.34 \times 10^{20}$ m^{-3}, where a/L_{Te}=3.452, a/L_{Te}=3.612, a/L_{ne}=a/L_{ni}=0.851, and $T_i/T_e = 0.385$.

$\nu_{ei}/(c_s/a)$	χ_e [m^2/sec]	χ_i [m^2/sec]
0.01	0.67	2.97
0.05	0.56	2.67
0.10	0.48	2.32

Similar linear stability analyses are performed in the planes of a/L_{Ti} - a/L_{Te} and a/L_{Ti} - T_i/T_e. The result in the planes of a/L_{Ti} - a/L_{Te} are shown in Fig. 16, where ITG remains the most unstable mode even after varying a/L_{Ti} and a/L_{Te} by 50%. The results in the planes of a/L_{Ti} - T_i/T_e are shown in Fig. 17, where ITG also remains the most unstable mode in the range of $a/L_{Ti} \geq 1.6$ and $0.2 \leq T_i/T_e \leq 1.0$.

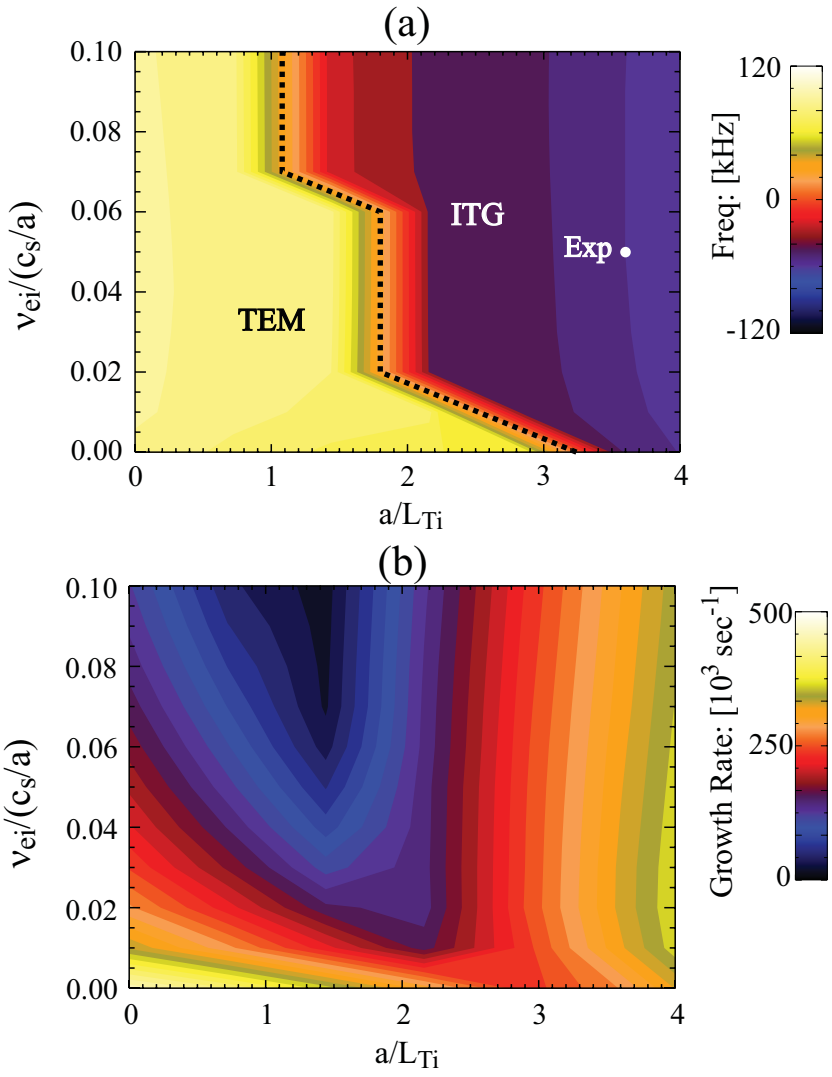

Figure 15: Contour plots of the frequency (a) and the growth rate (b) in the a/L_{Ti} - $\nu_{ei}/(c_s/a)$ plane. The other plasma parameters are taken from $r/a=0.63$ at the lowest density plasma with $\bar{n}_e=0.34\times10^{20}$ m^{-3}, where a/L_{Te}=3.452, a/L_{ne}=a/L_{ni}=0.851, and $T_i/T_e=0.385$. The linear stability calculation is performed at $k_\theta\rho_s\sim0.8$. The experimental values a/L_{Ti} and $\nu_{ei}/(c_s/a)$ are marked on the contour plot of the frequency, where the dashed line corresponds to the separation between the ITG mode ($f<0$) and the TEM (($f>0$)).

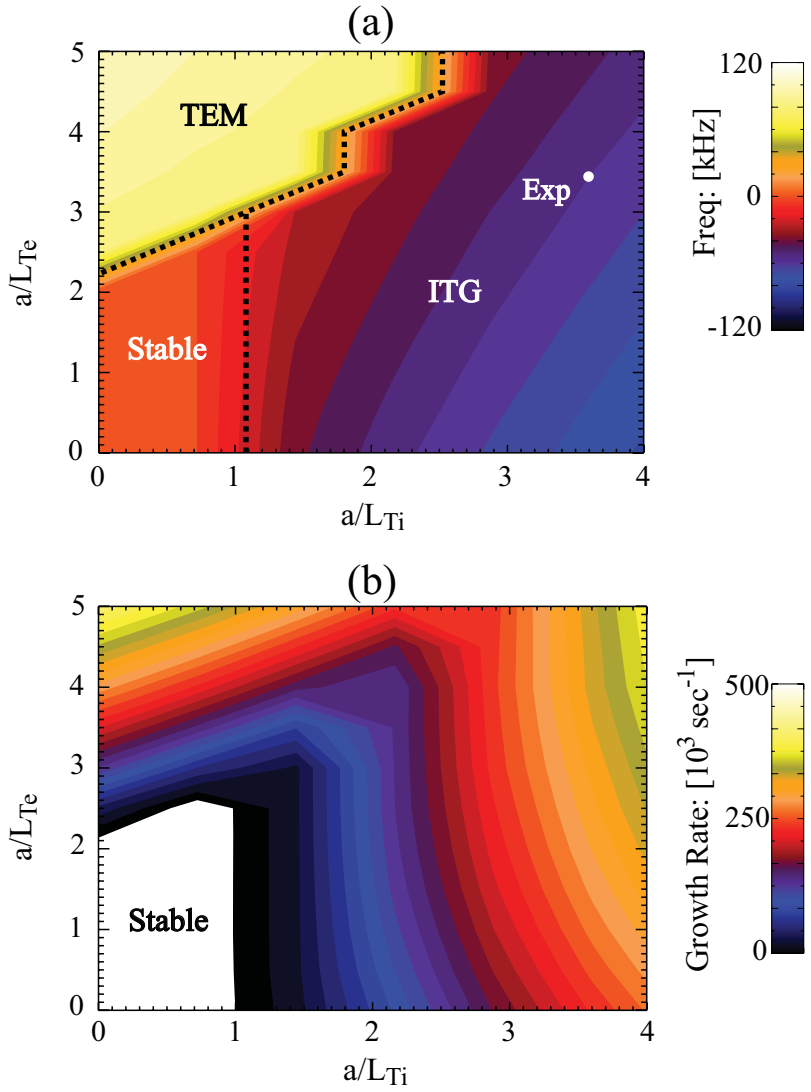

Figure 16: Contour plots of the frequency (a) and the growth rate (b) in the a/L_{Ti} - a/L_{Te} plane. The other plasma parameters are taken from $r/a = 0.63$ at the lowest density plasma with $\bar{n}_e = 0.34\times10^{20}$ m^{-3}, where a/L_{ne}=a/L_{ni}=0.851, $T_i/T_e = 0.385$, and $\nu_{ei}/(c_s/a) = 0.051$. The linear stability calculation is performed at $k_\theta\rho_s \sim 0.8$. The experimental values a/L_{Ti} and a/L_{Te} are marked on the contour plot of the frequency, where the dashed line corresponds to the separation between the stable regime, the ITG mode ($f < 0$), and the TEM (($f > 0$)).

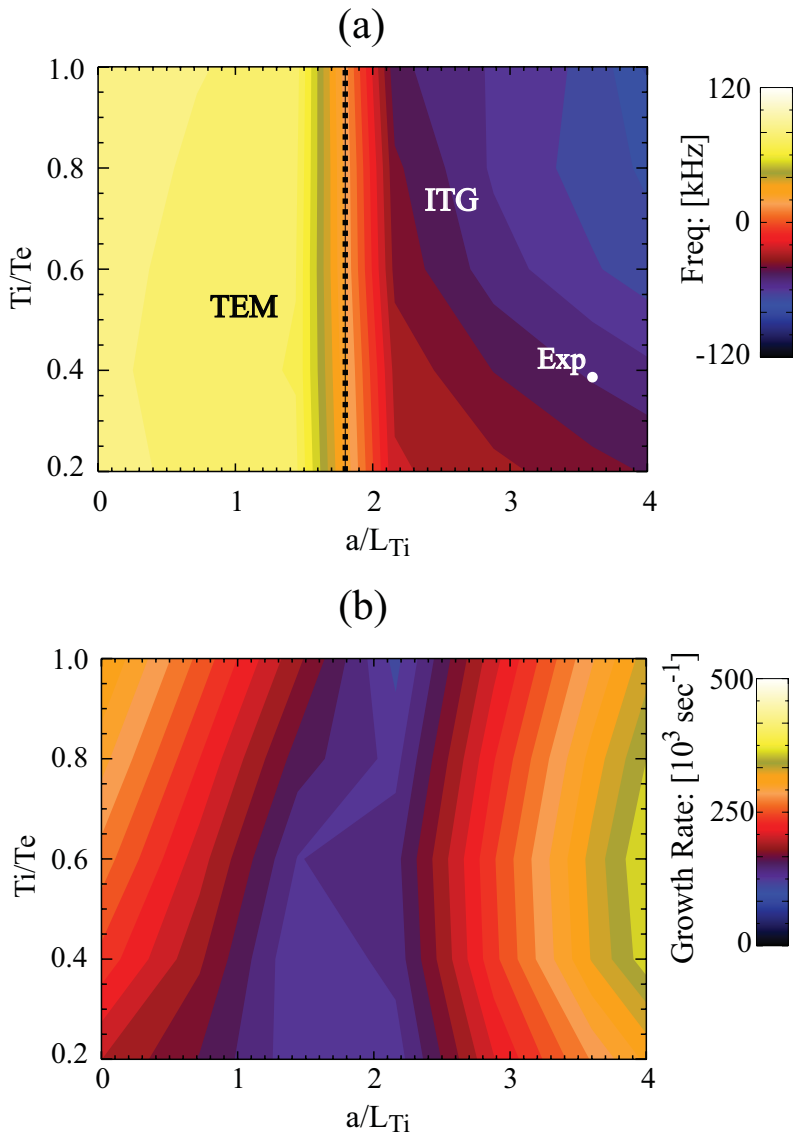

Figure 17: Contour plots in the a/L_{Ti} - T_i/T_e plane of the frequency at the maximum growth rate (a) and the maximum growth rate (b) in the wavenumber range of $0.4 \le k_\theta \rho_s \le 1.2$. The other plasma parameters are taken from $r/a = 0.63$ at the lowest density plasma with $\bar{n}_e = 0.34 \times 10^{20}$ m^{-3} , where $a/L_{ne} = a/L_{ni} = 0.851$, $a/L_{Te} = 3.452$, and $\nu_{ei}/(c_s/a) = 0.051$. The experimental values a/L_{Ti} and T_i/T_e are marked on the contour plot of the frequency, where the dashed line corresponds to the separation between the ITG mode ($f < 0$) and the TEM (($f > 0$)).

To further investigate the discrepancy at the lower density in the linear ohmic regime, we have also performed nonlinear GYRO simulations in the shorter wavelength length ($k_\theta \rho_s > 1.0$) regime. The linear stability analysis shows the unstable ETG with the growth rate spectra peaking at $k_\theta \rho_s \sim 25$ across the domain of $r/a = 0.63$. The nonlinear GYRO simulations include 16 modes up to $k_\theta \rho_s = 4$ at $\overline{n}_e = 0.34 \times 10^{20}$ m^{-3} with the real mass ratio ($m_i / m_e \approx 3600$) and kinetic electrons. The wavenumber spectra of the simulated electron and ion thermal transport are shown in Fig. 18. The contribution of the short wavelength turbulence in the range of $4.0 > k_\theta \rho_s > 2.0$ to the electron thermal transport is only 5.0% and its contribution to the ion thermal diffusivity is negligible.

Recent simulations with characteristic parameters of DIII-D core plasmas by Candy and Waltz [37, 38] shows that 10-20% of the total electron transport can arise from the ETG scale ($k_\theta \rho_s > 1.0$) where the ion-scale instabilities are not suppressed. They also showed that if the ion-scale instabilities are suppressed, by removal of the ion free energy [37] or by the presence of ExB shear suppression [38], this fraction can increase significantly. This result was also confirmed by Goerler and Jenko [39]. However, since the case we are considering has significant ITG drive, it seems unlikely that the ETG scale ($k_\theta \rho_s > 1.0$) turbulence can significantly contribute to the electron thermal transport. This has been partially verified by our simulations up to $k_\theta \rho_s = 4.0$, which shows that only 12.5% of the electron transport arises from the short wavelength turbulence in the range of $4.0 > k_\theta \rho_s > 1.0$. Nevertheless, in the future, it may be interesting to explore the role of even shorter wavelength turbulence in the range of $k_\theta \rho_s > 4.0$ under our experimental conditions and profiles to resolve this issue. Currently, we have not had access to expensive computer capabilities that are necessary for nonlinear GYRO simulation of such turbulence.

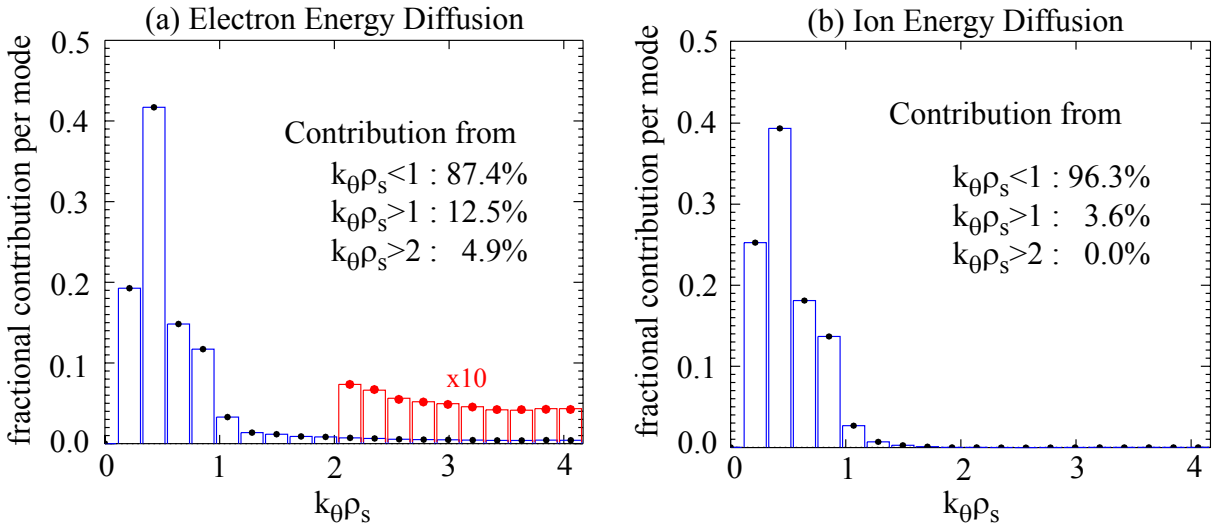

Figure 18. Fractional contribution per mode to thermal energy diffusion: (a) electron; (b) ion. The simulation is performed at $\overline{n}_e = 0.34\times10^{20}$ m^{-3} in the linear ohmic regime.

7. Summary and Discussion

In this paper, we reported numerical and experimental studies of turbulence and transport in Alcator C-Mod ohmic plasmas. The studies were carried out over the range of densities covering the "neo-Alcator" (linear confinement time scaling with density, electron transport dominates) to the saturated ohmic regime. Quantitative comparisons in both turbulence and thermal transport between experimental measurement and simulation were performed.

At high densities in the saturated ohmic regime, the key role played by the ITG turbulence has been verified, including measurements that the turbulent waves propagate in the ion diamagnetic direction. It is also found that the intensity of density fluctuations increases with density, in agreement between simulation and experiments. The absolute fluctuation wavenumber spectrum agrees with simulation within experimental error (+/-60%). Agreement in χ_e, χ_i, and χ_{eff} between experiment and theory is obtained after taking a 20% reduction of a/L_{Ti}, all within the experimental uncertainty.

At the low density in the linear ohmic regime, where the electron transport dominates ($\chi_e \gg \chi_i$), the GYRO simulation of the longer wavelength turbulence ($k_\theta \rho_s < 1$) shows $\chi_i > \chi_e$ although the simulated χ_{eff} agrees with experiments after reducing the ion temperature gradient by 20%.

Our nonlinear simulation including the shorter wavelength turbulence up to $k_\theta \rho_s \sim 4$ does not raise the simulated electron thermal diffusivity to the experimental level. Although it is possible that measurements and simulations at even shorter wavelengths may be necessary to explain transport in this regime, measurements to date by PCI indicate very low levels of high-k turbulence, falling into the background noise level. While the TEM modes are linearly unstable, under our experimental conditions their growth rates are smaller than the ITG modes. The nonlinear simulations of TEM turbulence would become important only for significantly steeper density gradients, namely a/L_n greater than about 2.5. Hence according to our nonlinear GYRO simulations, a significant thermal transport contribution from the TEM turbulence is not likely in the C-Mod low density ohmic regime. Our simulations including electromagnetic effects also show that the contribution from electromagnetic fluctuations is negligible in these low-β plasmas. Therefore, at the present time we are unable to determine the cause of the dominant electron transport in the linear ohmic regime. One possibility is turbulent energy exchange between electrons and ions;[40] this may be important in the low-density linear ohmic regime but has not been explored in our studies. Another possibility, not included in gyrokinetic simulations, is that the electron drift velocity associated with the "ohmic toroidal plasma current" drives electron drift waves which may be more unstable at the lower densities where the electron drift velocity can be a non-negligible fraction of the electron thermal speed and can even exceed the ion acoustic speed. To explore this would require a modification of present day gyrokinetic codes in use.

Acknowledgments

The authors want to thank the Alcator C-Mod physics staff and operations group for their contributions and support. The authors also wish to thank Mr. T. Baker and Drs. D. Ernst and J. Wright for implementing and maintaining the Loki cluster which is supported by the US SCIDAC theory program. We also want to thank Dr. D. Ernst for value discussions regarding gyrokinetic theory and code developments. This research utilized parallel computational clusters at MIT Plasma Science and Fusion Center (Loki) and Princeton Plasma Physics Laboratory (Kestrel). This work is supported by U. S. DOE under DE-FG02-94-ER54235 and DE-FC02-99-ER54512.

References

[1] Parker R R *et al* 1985 *Nucl. Fusion* **25** 1127
[2] Brower D L *et al* 1987 *Phys. Rev. Lett.* **59** 48
[3] Rettig C L *et al* 2001 *Phys. Plasmas* **8**, 2232
[4] Molvig K, Hirshman S P and Whitson J C 1979 *Phys. Rev. Lett.* **43** 582
[5] Coppi B 1980 *Comments Plasma Phys. Cont. Fusion* **5** 261
[6] Dominguez R R and Waltz R E 1987 *Nucl. Fusion* **27** 65
[7] Waltz R E, Dominguez R R and Perkins F W 1989 *Nucl. Fusion* **29** 351
[8] Waltz R E and Dominguez R R 1989 *Phys.* Fluids **B 1** 1935
[9] Weynants R R *et al* 1999 *Nucl. Fusion* **39** 1637
[10] M Z Tokar *et al* 1999 *Plasma Phys. Control. Fusion* **41** L9
[11] M Z Tokar *et al* 1999 *Plasma Phys. Control. Fusion* **41** B317
[12] A Kreter *et al* 2003 *Plasma Phys. Control. Fusion* **45** 199
[13] Angioni C *et al* 2005 *Phys. Plasmas* 12 040701
[14] Conway G D *et al* 2006 *Nucl. Fusion* **46** S799
[15] Porkolab M *et al* 2006 *IEEE Trans. Plasma Sci.* **34** 229
[16] Lin L *et al* 2006 *Rev. Sci. Instrum.* **77** 10E918
[17] Candy J and Waltz R E 2003 *J. Comput. Phys.* **186** 545
[18] Candy J and Waltz R E 2003 *Phys. Rev. Lett.* **91** 045001
[19] Dorland W, Jenko F, Kotschenreuther M, and Rogers B N 2000 *Phys. Rev. Lett.* **85** 5570
[20] Jenko F, Dorland W, Kotschenreuther M, and Rogers B N 2000 Phys. Plasmas **7** 1904
[21] Chen Y and Parker S 2007 *J. Comput. Phys.* **220** 839
[22] Lin Z *et al* 2007 *Plasma Phys. Contr. Fusion* **49** B163
[23] Rost J C *et al* 2007 *Bull. Am. Phys. Soc.* **52** (16) 334
[24] Lin L *et al* 2009 *Phys. Plasma* **16** 012502
[25] Greenwald M *et al* 2005 *Nucl. Fusion* **45** S109
[26] Basse N P *et al* 2007 *Fusion Sci. Technol.* **51** 476
[27] Goldston R J *et al* 1981 *J. Comput. Phys.* **43** 61
[28] Ince-Cushman A *et al* 2006 *Rev. Sci. Instrum.* **77** 10F321
[29] Fiore C L and Boivin R L 1995 *Rev. Sci. Instrum.* **66** 945
[30] Sauter O, Angioni C, and Lin-Liu Y R 1999 *Phys. Plasmas* **6** 2834
[31] Coda S, Porkolab M, and Carlstrom T N 1992 *Rev. Sci. Instrum.* **63** 4974
[32] Dorris J R, Rost J C and Porkolab M 2009 *Rev. Sci. Instrum.* **80**, 023503
[33] Tsujii N *et al* 2007 *Bull. Am. Phys. Soc.* **52** (16) 215
[34] Dimits A M *et al* 2000 *Phys. Plasmas* **12** 072304
[35] Waltz R E, Candy J, and Petty C 2006 *Phys. Plasmas* **7** 969
[36] Kinsey J E, Waltz R E, and Candy J 2007 *Phys. Plasma* **14** 102306
[37] Candy J, Waltz R E, Fahey M and Holland C 2007 *Plasma Phys. Contr. Fusion* **49** 1209
[38] Waltz R E, Candy J, and Fahey M 2007 *Phys. Plasma* **14** 056116
[39] Goerler T and Jenko F 2008 *Phys. Rev. Lett.* **100** 185002
[40] Waltz R E and Staebler G M 2008 *Phys. Plasma* **15** 014505